


Article

Study on the Effect of Microstructure Gradients Caused by Heat Gradients on Hydrogen Embrittlement Sensitivity in Heavy Forgings

Lingxiao Li , Jiyan Liu, Yuhao Wang, Guozhu Zhang and Fengshan Du *

National Engineering Research Center for Equipment and Technology of Cold Strip Rolling, Yanshan University, Qinhuangdao 066004, China; lingxiaoli7842115@163.com (L.L.); jiyanyanliu2@163.com (J.L.); 15940265196@163.com (Y.W.); aa13031872963@163.com (G.Z.)

* Correspondence: fsdu@ysu.edu.cn; Tel.: +86-13803354838

Abstract: The hydrogen embrittlement problem of alloy steel heavy forgings not only has the common properties of general hydrogen embrittlement, but also has the characteristics brought by its scale characteristics. The research of hydrogen embrittlement, combined with its characteristics and commonness, is of vital importance for the service safety of engineering structures. The temperature field and microstructure distribution in the machining process were investigated through the simulation of a finite element. On this basis, the physical simulation experiments were carried out to obtain the microstructure of heavy forgings in radial directions. The hydrogen embrittlement sensitivity was characterized by electrochemical hydrogen charging and slow strain rate tests (SSRT). The microstructure and fracture morphology of the samples were characterized to explore the law and mechanism of hydrogen embrittlement sensitivity gradient distribution along the axial direction. It is helpful to understand the hydrogen embrittlement of heavy forgings in order to guide engineering practice.

Keywords: heavy forgings; hydrogen embrittlement; finite element simulation; microstructure



Citation: Li, L.; Liu, J.; Wang, Y.; Zhang, G.; Du, F. Study on the Effect of Microstructure Gradients Caused by Heat Gradients on Hydrogen Embrittlement Sensitivity in Heavy Forgings. *Metals* **2022**, *12*, 610.

<https://doi.org/10.3390/met12040610>

Academic Editors:
Francesco Iacoviello and
Tomáš Prošek

Received: 14 February 2022

Accepted: 29 March 2022

Published: 1 April 2022

Publisher's Note: MDPI stays neutral with regard to jurisdictional claims in published maps and institutional affiliations.



Copyright: © 2022 by the authors. Licensee MDPI, Basel, Switzerland. This article is an open access article distributed under the terms and conditions of the Creative Commons Attribution (CC BY) license (<https://creativecommons.org/licenses/by/4.0/>).

1. Introduction

As a component of large equipment, heavy forgings are widely used in shipbuilding, metallurgy, manufacturing, and other industrial fields. Due to the poor service environment in which they exist, such as heavy load, alternating load and other complex mechanical conditions, the quality and safety of heavy forgings has been a bottleneck problem in the industrial field. The mechanical properties of the steel decrease due to the interaction of hydrogen with steel [1,2], and the sudden fracture failure of heavy forgings caused by hydrogen embrittlement often brings great security risks and economic losses. Therefore, it is of great engineering value and scientific significance to study the hydrogen embrittlement mechanism, as well as the hydrogen embrittlement sensitivity of heavy forgings.

Since the discovery of hydrogen embrittlement, many scholars have studied the mechanism of hydrogen embrittlement of steel. The hydrogen embrittlement of Cr5 backup roll has been a concern of many scholars [3,4] Fan et al. studied the effect of flaking on the hydrogen embrittlement of Cr5 material, increasing our understanding of flake formation and propagation mechanisms in Cr5 steel. A large number of studies [5–15] have proven that hydrogen embrittlement sensitivity is closely related to the microstructure of the steel in question. For instance, Michler et al. carried out hydrogen charging experiment and tensile tests on several industrial BCC steels with different structures, which were ferrite, pearlite, bainite, and martensite [5,6]. The results showed that different structures have different hydrogen embrittlement sensitivity. Ji, Kimura, et al. carried out a series of tests on tempered martensite and full pearlite hydrogen-charged samples with a tensile strength of 1600 MPa [7,8]. The results of SSRT showed that tempered martensitic steels were more prone to hydrogen delayed fracture than full pearlitic steels. Jeffrey et al. studied the

effect of microstructure on hydrogen embrittlement of high strength steels [9,10]. It was found that the sensitivity of different structures to hydrogen embrittlement was different. Bollinger, Martin, et al. studied the effect of microstructure on hydrogen embrittlement sensitivity [11,12]. The results showed that γ phase volume fraction and γ phase boundary area had significant effects on hydrogen absorption and hydrogen embrittlement sensitivity. Hejazi studied the hydrogen-induced cracking sensitivity of pipeline steels, and proved that there was a great difference in hydrogen embrittlement sensitivity caused by different microstructures [13]. Marchi, Hughes, et al. carried out hydrogen charging experiments on 304 L and 316 L austenitic stainless steels [14,15]. The results showed that significant ductility loss was observed in both metastable and stable alloys. Toribio studied the role of microstructural anisotropy in a hydrogen-assisted fracture. A markedly oriented microstructure was obtained using heavily drawn pearlitic steel wires. The influence of microstructural anisotropy in cold-drawn pearlitic steels on the hydrogen-assisted micro-damage path was analyzed in terms of the so-called tearing topography surface (TTS). Results revealed that hydrogen enhances the key role of the oriented microstructure in the anisotropic behavior [16,17].

The above studies have all proven the inseparable relationship between microstructure and hydrogen embrittlement sensitivity. For small-size parts, it is also easy to obtain uniform structure. However, the size of heavy forgings is too large, therefore it is difficult to obtain uniform structure. Especially during the heat treatment process, there will be a great difference between the external temperature and the internal temperature of the forgings, and the change of temperature in the machining process will lead to changes in the microstructure of the material. The non-uniformity of the overall temperature of forgings will cause the materials in different positions of forgings to show different to hydrogen embrittlement sensitivity, which will affect the service safety of forgings. To sum up, only by combining the microstructure distribution characteristics of the actual heavy forgings can we better explore the causes of hydrogen-induced crack initiation of heavy forgings and ensure their service safety.

For heavy forgings, the temperature gradient caused by the machining process will lead to differences in microstructure. Duan et al. [18] simulated the heat treatment process of heavy forgings by using finite element software. It was proven that different cooling methods will lead to different structures on the surface of forgings. Skubisz, Roumina, et al. studied the deformation behavior and microstructure response of medium-carbon high-strength steels at high strain rate and medium temperature, analyzed the hot workability and medium temperature workability of the material, and studied the effects of these factors on the microstructure after forging and direct cooling [19,20]. Hoseiny, Luo, et al. studied the microstructure and mechanical properties of 300 m forged steels, considered the temperature gradient in the process of aircraft landing gear forging and direct cooling, and analyzed the tensile properties and impact strength of different structures [21–23]. Zhu et al. had studied the effect of retained austenite on hydrogen embrittlement sensitivity of high-strength alloy steels under three different heat treatment conditions: quenching and partitioning (IAQP), quenching and partitioning (QP), quenching and tempering (QT). The results show that hydrogen embrittlement susceptibility increases in the following order: QT, QP and IAQP [24].

The large geometric characteristics of heavy forgings will inevitably lead to a large radial gradient of temperature field under limited heat transfer capacity. In addition, some special parts also require surface heat treatment, and the temperature difference between the core and the surface of the part will be larger. Therefore, for heavy forgings, considering only the material as a single factor is not suitable for the analysis of hydrogen embrittlement sensitivity, and a more accurate method is needed for hydrogen embrittlement sensitivity analysis of the internal structure of heavy forgings.

However, heavy forgings are extremely expensive. The direct detection of hydrogen embrittlement sensitivity of heavy forgings requires the destruction of heavy forgings. The ingenious use of computational simulation technology to build a suitable physical

simulation experiment can help to overcome this problem. This is an important way to study the hydrogen embrittlement of heavy forgings.

Therefore, aiming at the problem of hydrogen embrittlement of heavy forgings in engineering, this study used the combination of computer simulation, physical simulation experiments, and characterization experiments to explore the hydrogen embrittlement sensitivity of internal structure of heavy forgings, and analyzes the mechanism of hydrogen embrittlement sensitivity gradient formation combined with microstructure. Specifically, the finite element simulation was carried out for the post-forging heat treatment process, which produces microstructural gradient characteristics for heavy forgings. Gradient temperature fields along the radial direction generated during the forming process of heavy forgings were obtained. According to the temperature gradient, a set of characteristic points were selected along the radial direction to complete the heat treatment with the temperature change at this point, in order to obtain a set of samples which were close to the radial distribution of the microstructure of heavy forgings. The hydrogen embrittlement sensitivity was characterized by an SSRT test, and the variation of hydrogen embrittlement sensitivity along the radial direction of heavy forgings was obtained. The mechanism was explained through fracture and microstructure analysis. This study is helpful to guide the hydrogen embrittlement protection of heavy forgings, and to promote the application of hydrogen embrittlement mechanism research in engineering practice.

2. Research Methods

2.1. Finite Element Simulation of Heat Treatment Temperature Gradient Characteristics of Heavy Forgings

Aiming at tackling the problem of hydrogen embrittlement of heavy forgings under gradient characteristics, this study takes large shaft parts as the research object, which are made of Cr5 steel. The chemical composition of steel is shown in Table 1. The geometric model was established according to the actual heavy shaft parts. Due to the large size of heavy forgings, it was difficult to realize full vacuum treatment. Therefore, the main heat transfer modes in the heat treatment process of heavy forgings were the heat conduction inside the forgings, as well as the convective and radiative heat transfer between the forgings and the medium. The temperature field obeys the first law of thermodynamics and Fourier law in the whole process of heat conduction. The Fourier formula is:

$$\operatorname{div}(k \cdot \operatorname{grad}T) = \rho_1 C_P \left(\frac{\partial T}{\partial t} \right) \quad (1)$$

where k is heat flux density, and $\operatorname{grad}T$ is temperature gradient.

Table 1. Chemical composition of Cr5 steel.

Elements	C	Si	Mn	Cr	Mo	V	Fe
Contents (wt%)	0.56	0.46	0.69	5.12	0.47	0.14	Balance

The heat transfer of forgings in the process of heat treatment was more complex. In this study, the comprehensive heat transfer boundary can be expressed as follows:

$$\begin{aligned} -\lambda \frac{\partial T}{\partial n} \Big|_S &= H_k(T_w - T_c) + \sigma \varepsilon (T_w^4 - T_c^4) \\ &= H_k(T_w - T_c) + H_s(T_w - T_c) \\ &= H(T_w - T_c) \end{aligned} \quad (2)$$

where H is heat transfer coefficient.

$$H = H_k + H_s \quad (3)$$

H_s is radiative heat transfer coefficient.

$$H_s = \sigma \varepsilon (T_w^2 + T_c^2) (T_w + T_c) \quad (4)$$

σ is the Stefan–Boltzmann constant, and ε is workpiece surface radiance.

The heat transfer coefficients of materials in different heat treatment processes were measured by Gleeble-3800 thermal simulation machine, and the results obtained are similar to those reported in the literature [25,26]. The heat transfer coefficients of Cr5 steel during heating, air cooling, and spray cooling are shown in Figure 1a–c.

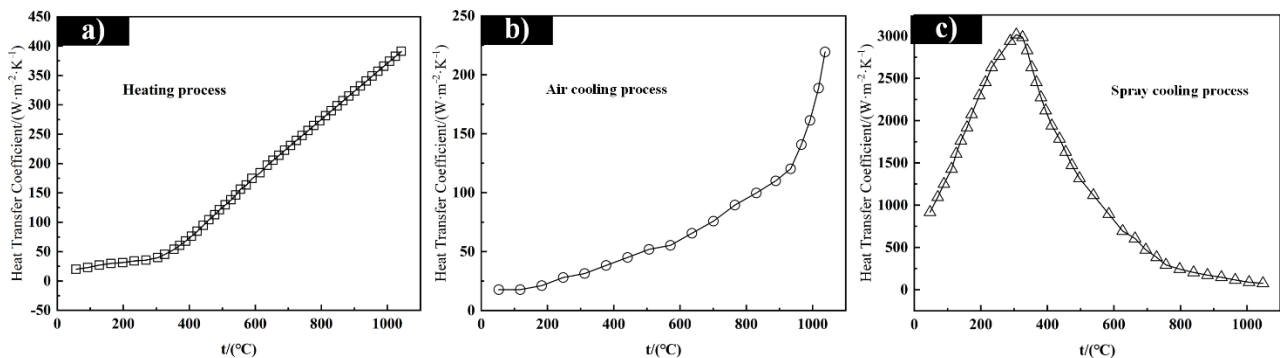


Figure 1. Heat transfer coefficient of Cr5 steel in different processes. (a) Heat transfer coefficient in heating process; (b) heat transfer coefficient in air cooling process; (c) heat transfer coefficient in spray cooling process.

The forging temperature and process of Cr5 steel are referenced in this paper, and the thermal physical parameters of Cr5 steel were measured with a TC-7000H laser thermal constant tester. The non-static test method was adopted to improve the measurement accuracy. The Cr5 steel samples were processed into a circular sheet of $\Phi 10 \text{ mm} \times 1.5 \text{ mm}$, and the surfaces were polished to a smooth surface. After the vacuum reached $1.3 \times 10^{-2} \text{ MPa}$, the samples were heated to the specified temperature at the rate of $10 \text{ }^\circ\text{C}/\text{min}$. After the temperature was stable, the samples were measured three times, and the average value was taken. The final thermophysical parameters of Cr5 steel are shown in Table 2.

Table 2. Thermophysical parameters of Cr5 steel.

Temperature (K)	Coefficient of Linear Expansion ($10^{-6}/\text{K}$)	Specific Heat Capacity (J/g·K)	Elastic Modulus (GPa)	Shear Modulus (GPa)	Thermal Conductivity (W/m·K)	Density (Kg/m ³)
300	14.6	0.528	189	73.5	41.67	7763
400	14.1	0.599	184	70.6	37.62	7745
500	15	0.698	172	66.6	34.17	7718
600	14.9	0.805	139	-	31.38	7691
700	14.9	0.993	93.3	-	29.45	7664
800	15.4	0.945	81.3	-	26.86	-
900	30.2	0.734	41.7	-	-	-
1000	26.2	0.747	29.9	-	-	-
1100	24.1	0.587	17.4	-	-	-

In this study, finite element software was used to simulate the heat treatment of forgings, and the third kind of boundary conditions were adopted. The finite element simulation for shaft parts of heavy forgings was carried out on the commercial software Design Environment for Forming (DEFORM[®] is developed by American Scientific Forming Technologies Corporation, Columbus, OH, USA). DEFORM[®] software is a finite

element-based process simulation system for analyzing various forming processes and heat treatment processes in metal forming and related industries. It can simulate normalizing, annealing, quenching, tempering, carburizing, and other processes, as well as predict hardness, grain structure composition and other functions. The material of shaft parts was considered to be single and uniform. The grids were divided automatically by the software, and the calculation accuracy was improved by refinement of the grid under the condition of ensuring convergence. Since the shaft parts were symmetrical, in order to reduce the amount of calculation, this study simplifies the parts into a two-dimensional model for simulation calculation. The dimensions and geometric characteristics of large shaft forgings are shown in Figure 2a. Figure 2b shows the specific objects of the forgings. According to the dimension and spatial symmetry of the forgings, the two-dimensional model was simplified and meshed on the DEFORM[®] software, as shown in Figure 2c. The model selects five reference points, A, B, C, D and E, from outside to inside in the radial direction of the part. That is, on the radial plane of the red line in Figure 2a, five points are uniformly (at 275 mm intervals) selected from the outer surface to the center of the cylinder. Point A was marked on the outer surface, and point E is the center of the cylinder. The temperature gradient along the radial direction during the heat treatment of heavy forgings was replaced by five reference points to facilitate the subsequent the analysis of hydrogen embrittlement sensitivity in different positions along the radial distribution.

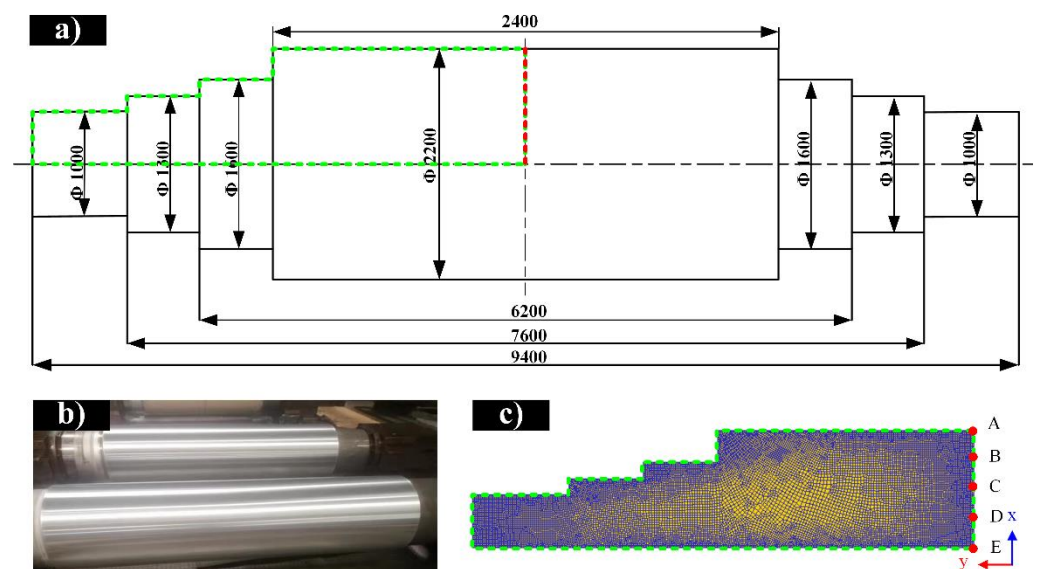


Figure 2. Geometric dimension and finite element model of heavy forging. (a) Geometric features and dimensions of forgings; (b) physical drawing of heavy forgings; (c) grid division diagram of forging DEFORM[®] model.

Overall, five parts of Cr5 steel were prepared from a piece of Cr5 steel, and they represented five sample points (A–E). The curves of temperature changes at five locations with the time obtained by the finite element simulation were used as heat treatment parameters to perform heat treatment operations on five groups, respectively. The curves of temperature changes at five locations with the time is determined by the heat treatment results.

2.2. Preparation and Characterization of Samples

Backup roll Cr5 steel was widely used as a material for large shaft parts. The heat treatment of the material was carried out in the heating furnace. The heat treatment process was controlled according to the temperature field of the selected point, in order to obtain each point samples and further experimental study. After heat treatment, rectangular cross-section tensile specimens were prepared using a wire cutting machine. A dogbone-shaped tensile test sample with a gauge length of 25 mm and width of 6 mm and its thickness was

1.6 mm. Tensile samples are designed according to national standards (NACE Standard TM 0198-2004).

The microstructure of samples with different heat treatment processes was characterized by the metallographic etching method. The sample surfaces are mechanically polished to the mirror surface, using 4% nitric acid ethanol solution as an etching agent, and etching for 20s at room temperature. After the corrosion is completed, the surfaces were cleaned with a 99.99% ethanol solution. The microstructure obtained by optical microscopy. The crystal orientation and size of the samples were characterized by electron backscattering diffraction (EBSD). In addition, the dislocation density was calculated from the kernel average misorientation (KAM). The scanning electron microscope experiment was carried out on a FEI-SCIOS scanning electron microscope. In order to ensure the measurement accuracy, the scanning step was 0.2 μm , the scanning voltage was 20 kV, and the current is 13 nA. Under the FEI-SCIOS scanning electron microscope, the fracture surfaces of the tensile samples were observed by scanning voltage 20 kV and current 6.4 nA.

2.3. Evaluation of Hydrogen Embrittlement Sensitivity

Hydrogen embrittlement samples were prepared through the electrochemical hydrogen charging method. In the electrolytic hydrogen charging experiments, 99.99% platinum electrode was used as an anode, and the sample as a cathode. The composition of the hydrogen charging electrolyte was 0.5 mol/L H_2SO_4 + 3.84 mmol/L Na_2S . The CS electrochemical workstation was used to provide hydrogen charging current. The current density used for hydrogen charging was 100 mA/cm^2 , and the temperature was 25 $^\circ\text{C}$. The duration of hydrogen charging for all samples was all 60 min. The tension experiment was carried out in 30 min after electrolytic hydrogen charging, and the SSRT was used to characterize the mechanical properties of the sample under the hydrogen charging process. The experiment was carried out on the Zwick Roell Z100 universal tensile testing machine. According to the ASTM G129-00 standard, the strain rate is taken as $1 \times 10^{-5}\text{s}^{-1}$ [27–29]. The average values of five groups of samples were taken for the same process parameters to eliminate random errors.

3. Results and Discussion

3.1. Temperature Field Gradient Characteristics of Heavy Forgings

The heat treatment process of Cr5 steel support shaft was referenced in this paper, and the heat treatment parameters of “spheroidizing annealing + tempering” were written into the finite element software for simulation. The whole heat treatment process is shown in Figure 3a, and the temperature cloud diagram of each stage is shown in Figure 3b. It can be seen from the figures that, during the whole process of heat treatment of forgings, the radial gradient characteristics of forgings are obviously shown, and the temperature of the outside of the forgings varies greatly in each stage. The temperature change of the whole heat treatment process of the extraction mark points A–E is shown in Figure 4a. The temperature curve of the internal point obtained by the finite element can simulate the change of the internal temperature in the actual process. The obtained temperature curves were used as the heat treatment process for each sample, respectively, and the heat treatment operation was performed on the five groups of samples. Figure 4b–e show the volume fraction of the microstructure content of point A with the whole heat treatment time. Points B–E on the inside of the forging show the same microstructure change. There is almost no martensite and austenite inside the forging, only pearlite and ferrite. Point A on the outside of the forging shows different microstructure changes from other points. The heat treatment process of heavy forgings can be regarded as the process of producing different structures in the radial direction of heavy forgings.

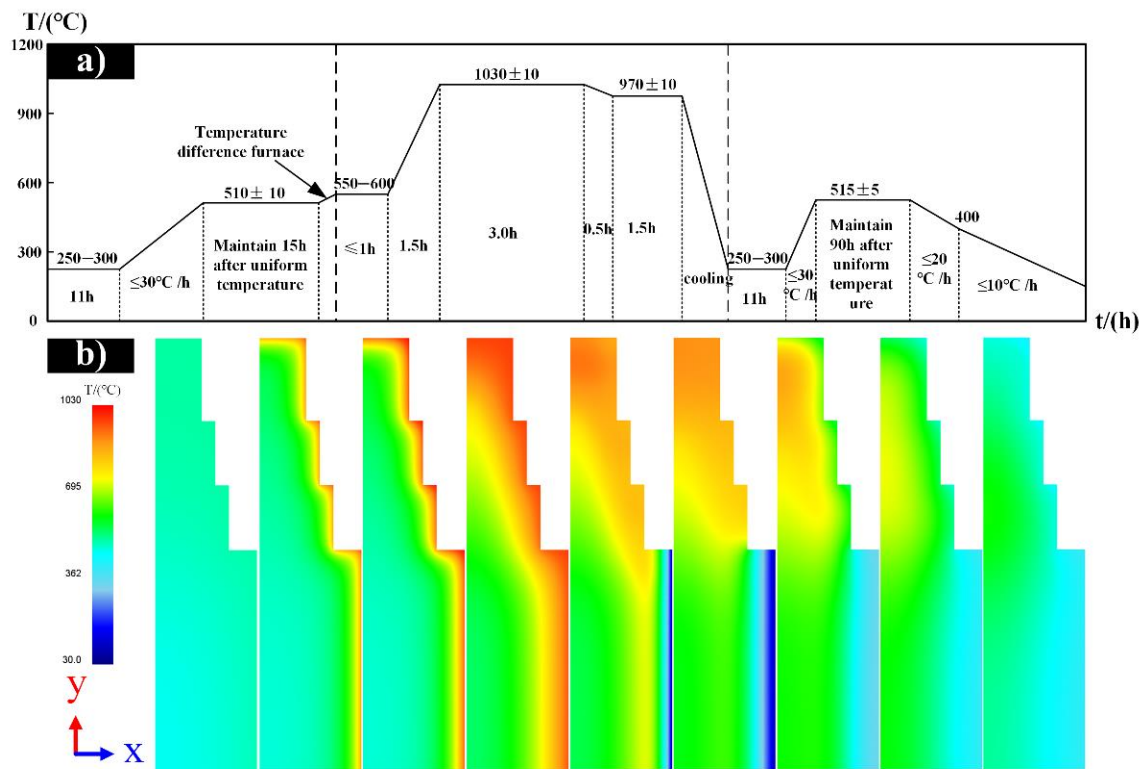


Figure 3. Heat treatment process and finite element simulation. (a) The whole process of heat treatment; (b) temperature cloud diagram of finite element simulation of forgings in different stages.

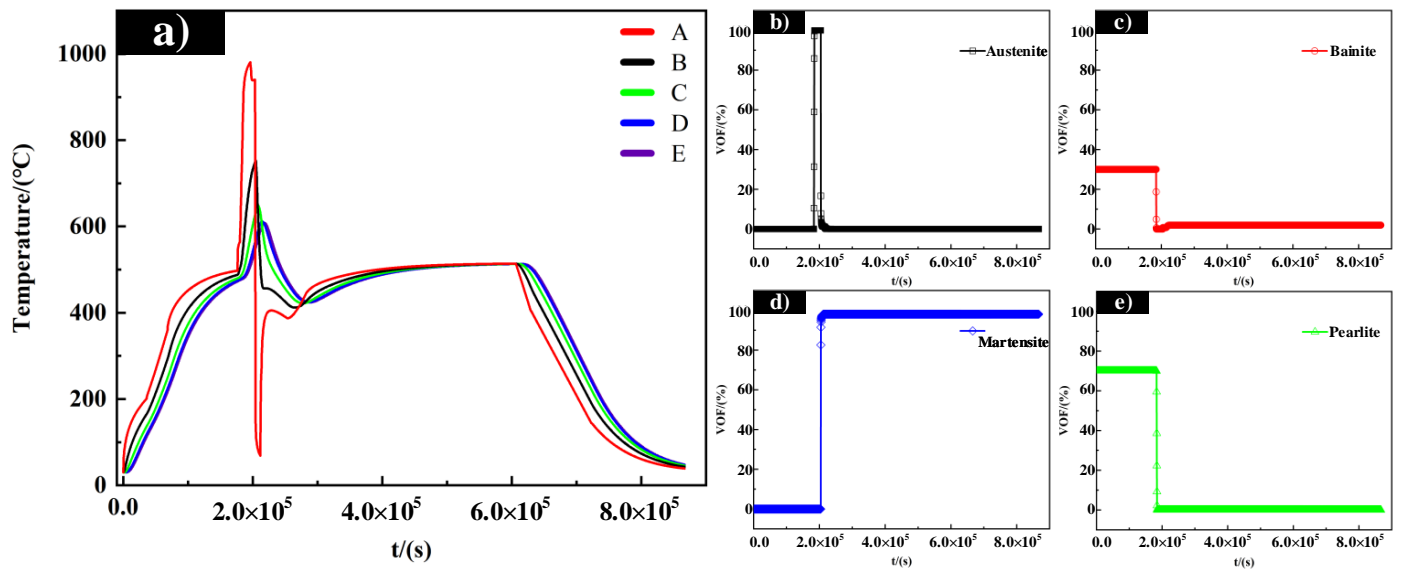


Figure 4. The temperature change diagram of heat treatment and the volume fraction of microstructure at each point. (a) The temperature change at each point of A–E during the whole heat treatment process; (b) the change of volume fraction of austenite content at point A with time; (c) the change of volume fraction of bainite content at point A with time; (d) the change of volume fraction of martensite content at point A with time; (e) the change of volume fraction of pearlite content at point A with time.

The cloud diagrams of the microstructure distribution of austenite, pearlite, and bainite before spray cooling are given in Figure 5a–c, respectively. When the backup roller is heated at a differential temperature, there is a huge temperature difference between the surface and the core, which leads to the difference in the radial microstructure. At the end of this process, a certain thickness of austenite was formed on the surface of the backup roll, since the surface position reached the phase transformation temperature. At this time, the core temperature did not reach the phase transformation, and the microstructure was still composed of pearlite and bainite with high toughness. From the cloud diagrams of microstructure distribution, it can be seen that the distribution of austenite on the surface of the backup roll is highly uniform. The roll body of the backup roll has reached the thickness of 200 mm, which is ready for the next step of spray cooling. It meets the technological requirements of differential temperature heating. When spray cooling is carried out, it is necessary to set aside a distance on both sides of the roll body of heavy forgings not to cool spray, so as to prevent shoulder loss.

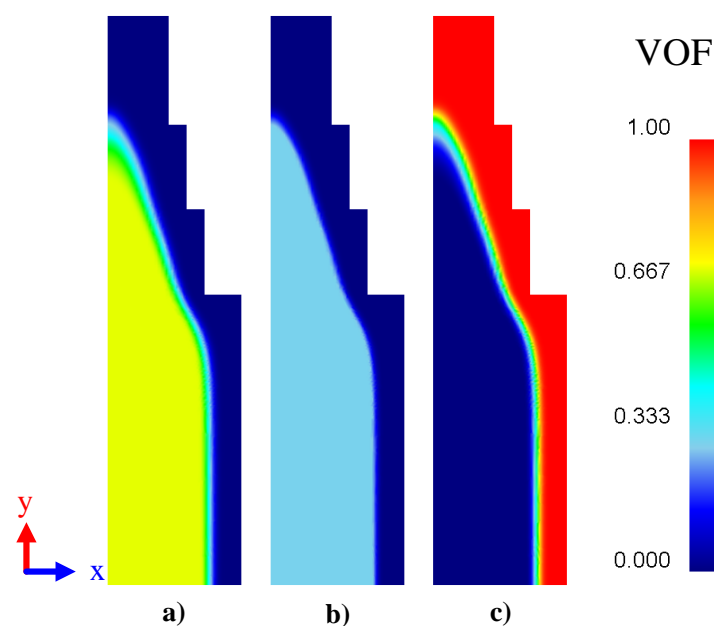


Figure 5. Cloud diagram of microstructure distribution before spray cooling. (a) Pearlite; (b) bainite; (c) austenite.

The cloud maps of the microstructure distribution of the backup roller after spray cooling are given in Figure 6a–c, respectively. After spray cooling of the backup roll, the temperature on the surface drops rapidly, while the core still measures a high temperature. After the start of spray cooling, the surface temperature of the backup roll changes very sharply, and a certain thickness of martensite will be formed rapidly. In the subsurface layer, there will be a certain amount of bainite. The reason for this is that, during spray cooling, the temperature of the outermost layer decreases very quickly, while the temperature of the subsurface layer decreases slowly, and a part of the austenite is transformed into bainite, forming a bainite layer in the roll body. There is almost no phase transition from the outermost 200 mm of the roll body. The core structure of the forging is still pearlite.

According to the temperature results of the finite element simulation, the five groups of samples were respectively subjected to heat treatment operations, and the specific heat treatment processes corresponded to the temperatures at each point, as shown in Figure 4a. The microstructure morphology of five groups of samples after picric acid etching are shown in the Figure 7. The results show that the microstructure at point A outside the forging is martensite, the microstructure at point B is martensite and bainite, and the microstructure at points C, D, and E inside the forging is pearlite. The formation of the needle-shaped martensite at point A was due to the large degree of under-cooling

caused by spray cooling—the solid solution of carbon atoms in austenite has no time to diffuse out of the cell. For point B, the under-cooling degree was lower than point A. This means that the austenite was undercooled to a temperature lower than the pearlite transformation temperature and higher than the martensite transformation temperature. The transformation of austenite will be coordinated by shear transformation and short-range diffusion. This led to the microstructure of martensite and bainite in point B. With regard to points C, D, and E, the pearlite structure is retained at these positions due to incomplete austenitization. Therefore, it can be found that the microstructure obtained by heat treatment is consistent with the simulation results in this paper, and the accuracy of the simulation in this paper is proved.

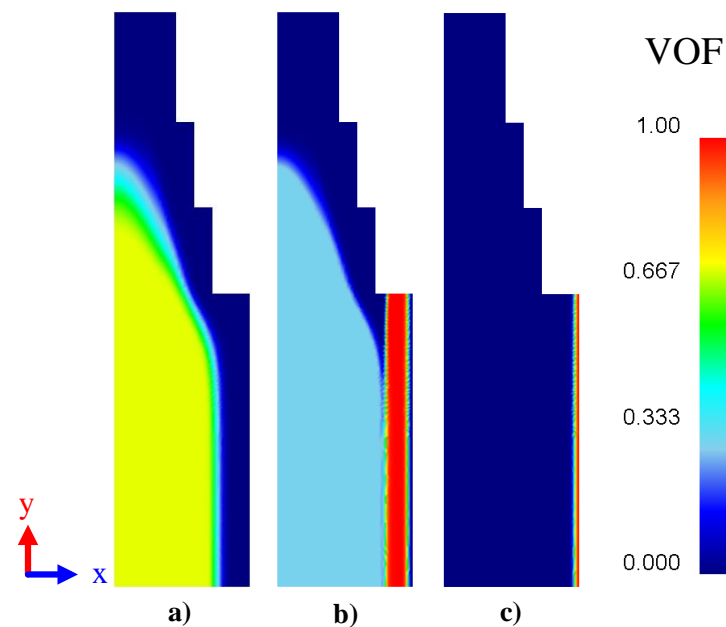


Figure 6. Cloud diagram of microstructure distribution after spray cooling. (a) Pearlite; (b) bainite; (c) martensite.

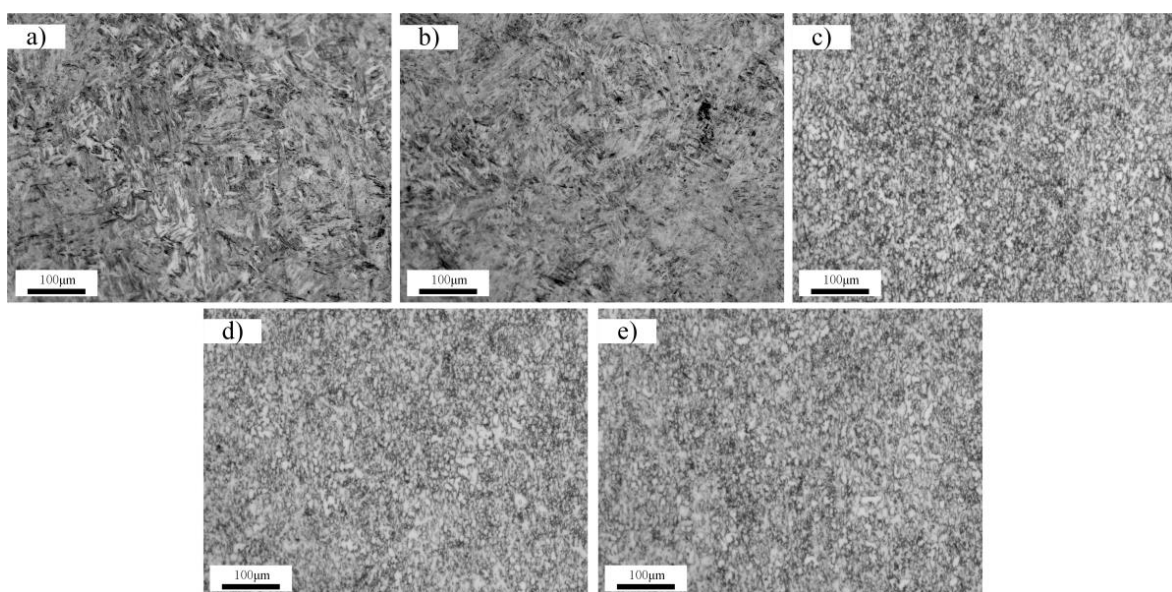


Figure 7. Microstructure of each sample after etching. (a) Microstructure of sample A; (b) microstructure of sample B; (c) microstructure of sample C; (d) microstructure of sample D; (e) microstructure of sample E.

3.2. Results of Hydrogen Embrittlement Sensitivity

With reference to the time-varying temperature curve of each point in the finite element simulation (Figure 4a), the Cr5 steel with the same composition as the heavy forging was heat-treated according to the temperature change of the A–E points, and the experimental samples matched with the A–E points process were obtained. The strength and plasticity of five groups of the A–E samples after electrolytic hydrogen charging are shown in Figure 8. At the same time, error bars for repeated trials are marked on each point. The projection of the two-point connection line on the abscissa before and after hydrogen charging reflects the hydrogen-induced plasticity loss of the sample.

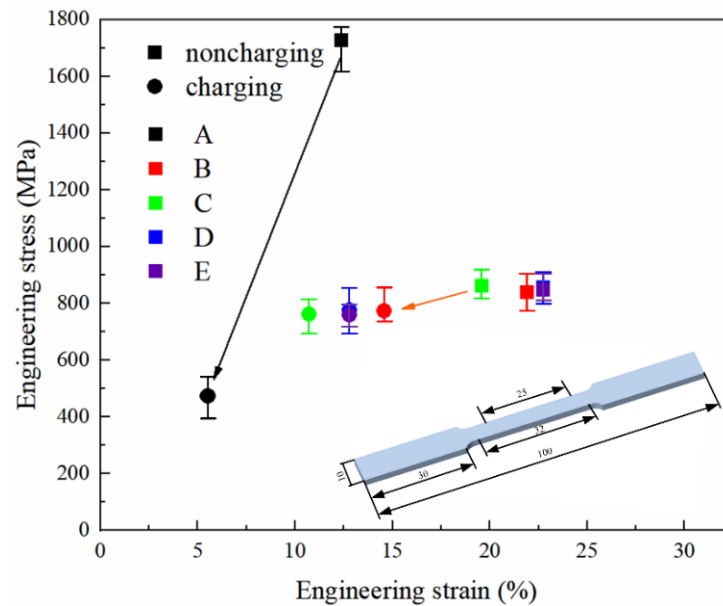


Figure 8. Comparison of the changes in strength and ductility of each group of materials before and after electrolytic hydrogen charging.

The index of hydrogen embrittlement sensitivity of metallic materials can accurately reflect the sensitivity of materials to hydrogen embrittlement. Through the SSRT test, the sensitivity index of materials is usually calculated by formula Equations (5) and (6):

$$I_{\psi} = (\psi_O - \psi_H) / \psi_O \times 100\% \tag{5}$$

$$I_{\delta} = (\delta_O - \delta_H) / \delta_O \times 100\% \tag{6}$$

where I_{ψ} is the index of hydrogen embrittlement sensitivity expressed by reduction of area(RA), ψ_O is the RA without hydrogen charge, ψ_H is the RA after hydrogen charging, I_{δ} is the hydrogen embrittlement sensitivity index expressed by elongation(EL), δ_O is expressed as the EL of uncharged hydrogen, and δ_H is expressed as the EL after hydrogen charging. The hydrogen embrittlement sensitivity of steel can be clearly reflected by comparing the values of I_{ψ} and I_{δ} . The results of the EL, RA, and hydrogen embrittlement sensitivity index of each group of materials are shown in Tables 3–5, respectively.

Table 3. EL of different samples.

-	A	B	C	D	E
Non-hydrogen charging (%)	23.38	26.91	29.61	27.75	27.74
Hydrogen charging (%)	9.03	17.58	13.74	15.80	15.81

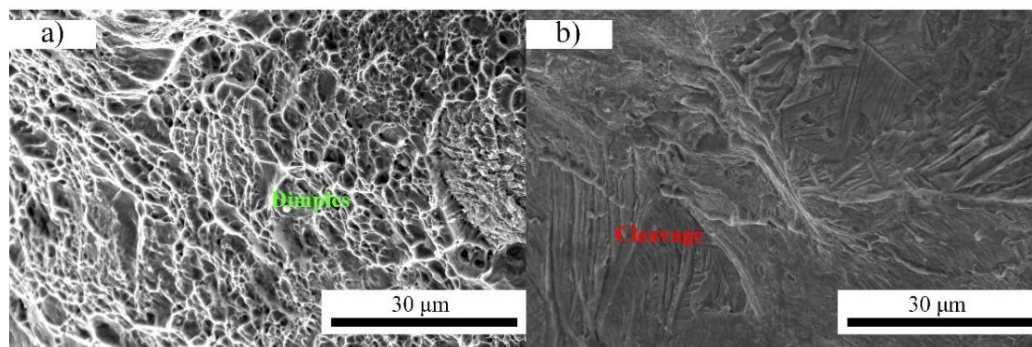
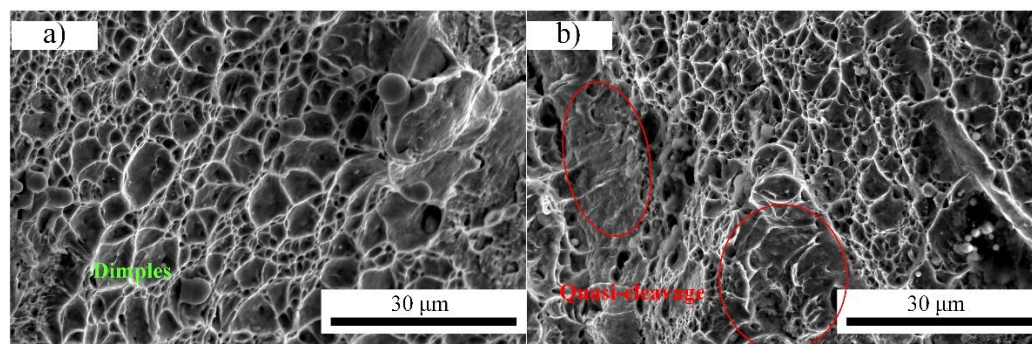
Table 4. RA of different samples.

-	A	B	C	D	E
Non-hydrogen charging (%)	17.77	14.69	10	14.52	16.88
Hydrogen charging (%)	1.08	6.03	1.27	3.89	4.82

Table 5. Hydrogen embrittlement sensitivity index of different samples.

-	A	B	C	D	E
I_{ψ} (%)	93.9	58.95	87.3	73.2	71.44
I_{δ} (%)	61.38	34.67	53.60	43.06	43.01

According to the data in Tables 3–5, the loss rate of hydrogen-induced plasticity of the samples from largest to smallest were A, C, E, D, and B, respectively. The hydrogen embrittlement sensitivity index of the five groups of samples corresponds to the five reference points in the finite element simulation of heavy forgings, and the SSRT and hydrogen embrittlement sensitivity indexes of hydrogen-charged and uncharged samples were compared. The EL of sample A decreased by 94%, and the RA decreased by 61%, which indicated that the hydrogen embrittlement of sample A was the highest. The degree of hydrogen embrittlement of sample C is also significant, the degree of hydrogen embrittlement of samples D and E is similar and lower than that of sample C, and the degree of hydrogen embrittlement of sample B is the lowest. In order to further analyze the hydrogen embrittlement sensitivity of the samples, we characterized the fracture morphologies of five groups of samples with and without hydrogen charging. The cross-sectional morphologies of five groups of samples under SEM after SSRT are shown in Figures 9–13.

**Figure 9.** Slow-strain rate tensile fracture of samples A with and without hydrogen charging. (a) Not hydrogenated; (b) hydrogenated.**Figure 10.** Slow-strain rate tensile fracture of samples B with and without hydrogen charging. (a) Not hydrogenated; (b) hydrogenated.

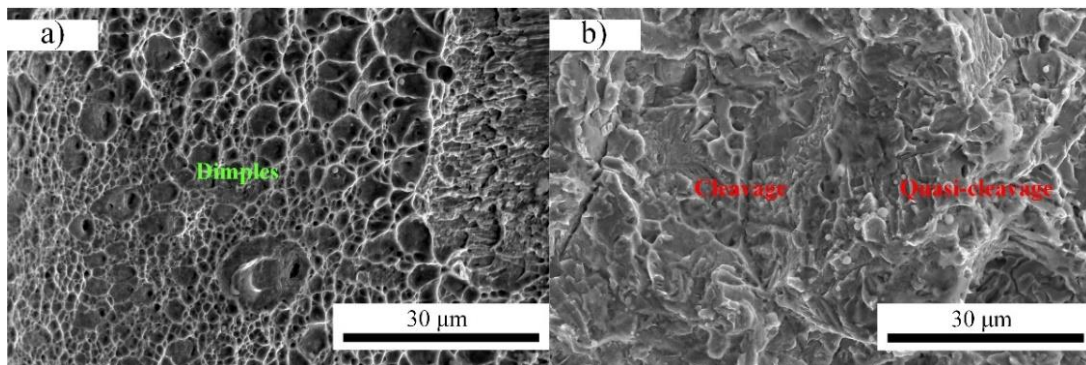


Figure 11. Slow-strain rate tensile fracture of samples C with and without hydrogen charging. (a) Not hydrogenated; (b) hydrogenated.

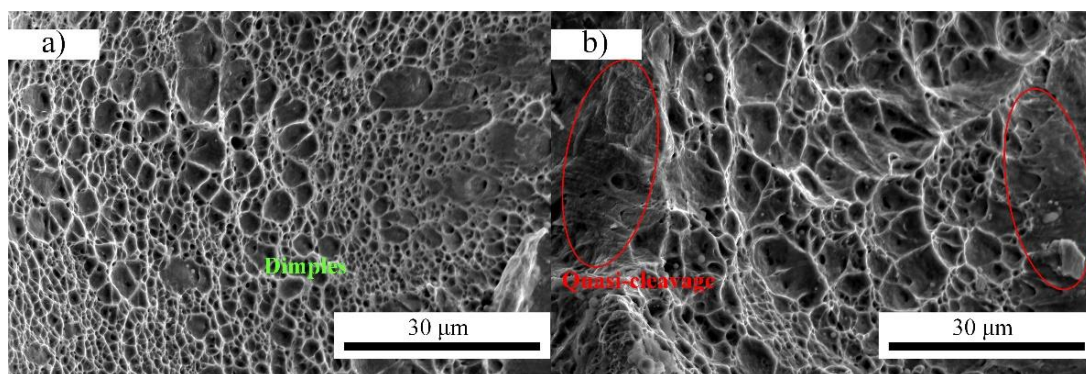


Figure 12. Slow-strain rate tensile fracture of samples D with and without hydrogen charging. (a) Not hydrogenated; (b) hydrogenated.

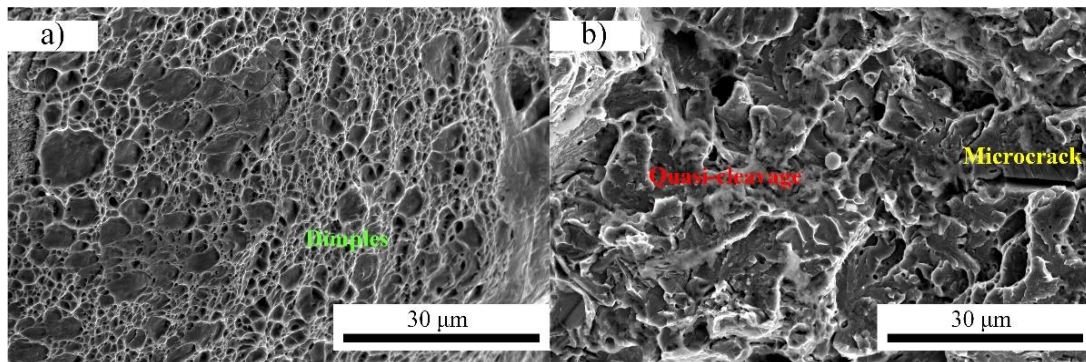


Figure 13. Slow-strain rate tensile fracture of samples E with and without hydrogen charging. (a) not hydrogenated; (b) hydrogenated.

In order to further analyze the hydrogen embrittlement sensitivity of the samples, we characterized the fracture morphologies of five groups of samples with and without hydrogen charging. The cross-sectional morphologies of five groups of samples under SEM after SSRT are shown in Figures 9–13. Figures 9a, 10a, 11a, 12a and 13a are the tensile fractures of the five groups of samples without hydrogen, respectively, Figures 9b, 10b, 11b, 12b and 13b are the fracture surfaces of hydrogen-charged samples, respectively. A large number of dimples can be observed in the fracture morphology of all the samples not filled with hydrogen. The fracture of the dimple morphology proves that the fracture form is a ductile fracture, but there is an obvious difference in the fracture surface after hydrogen charging. After hydrogen charging, the fracture surface of sample A shows obvious river morphology, which is a typical transgranular fracture. When the fracture surfaces of

samples C and E are observed, obvious intergranular cracks and high-density tearing edges can be observed, and some quasi-cleavage platforms appear on the fracture surface, which is obviously a mixed fracture. There was no significant change in the fracture surface of group B after hydrogen charging, compared with that of the non-hydrogen charging group. A large number of dimples appeared after hydrogen charging on the fracture surface of sample D, and the dimple depth of the fracture surface of sample D was relatively shallow compared with the group without hydrogen charge. The comparative observation and analysis of fracture morphology further proved that the hydrogen embrittlement sensitivity of the group B samples was lower, while that of the group A samples was the highest. Although the fractures of the BDE samples showed obvious ductile fractures, some quasi-cleavage platforms appeared locally.

The EBSD results of the five groups of samples are collected in Figures 14–18, for a better discussion on the influence of grain boundary and dislocation on hydrogen embrittlement. From the orientation map in Figures 14a, 15a, 16a, 17a and 18a and the statistical map of grain area in Figures 14c, 15c, 16c, 17c and 18c, it can be clearly seen that samples in group A have the smallest grain size, compared groups B, C, D, and E, due to the cooling rate being significantly lower than that of group A, which provides the driving force for grain growth. This makes the latter groups' average grain size larger than that of the group A samples. Geometrically necessary dislocation (GND) of the five groups of samples is calculated and shown in Figures 14b, 15b, 16b, 17b and 18b. GND is defined as the quantitative calculation of the average orientation difference and step size between the reference point and its adjacent points belonging to the same grain, which can be used to measure the dislocation situation. It is clear from the GND map that the dislocation density of the five samples is A, B, C, E, and D, from highest to lowest.

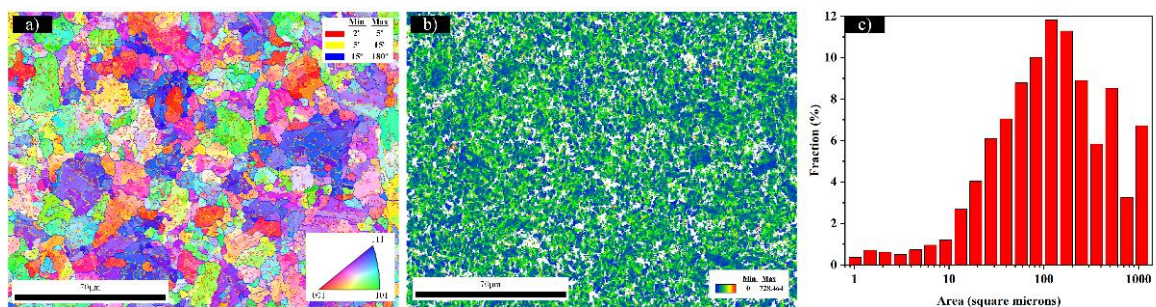


Figure 14. Microstructure information of sample A. (a) EBSD orientation map; (b) GND map; (c) grain area distribution.

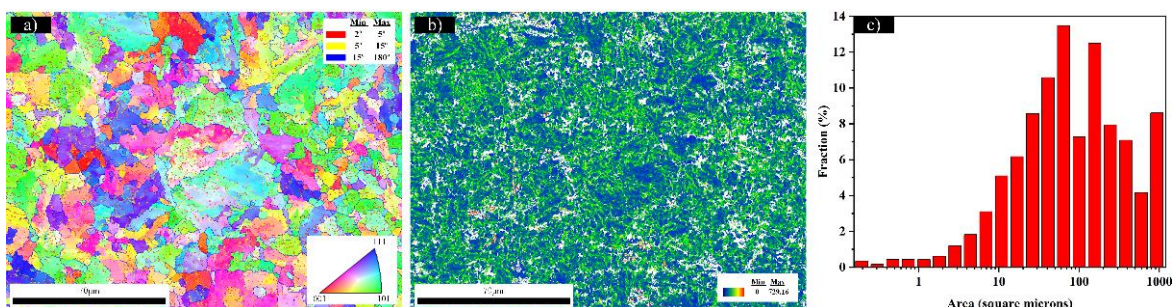


Figure 15. Microstructure information of sample B. (a) EBSD orientation map; (b) GND map; (c) grain area distribution.

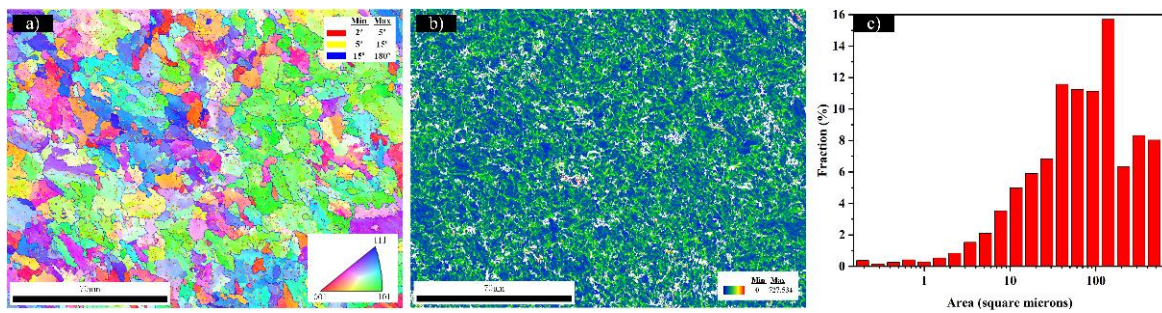


Figure 16. Microstructure information of sample C. (a) EBSD orientation map; (b) GND map; (c) grain area distribution.

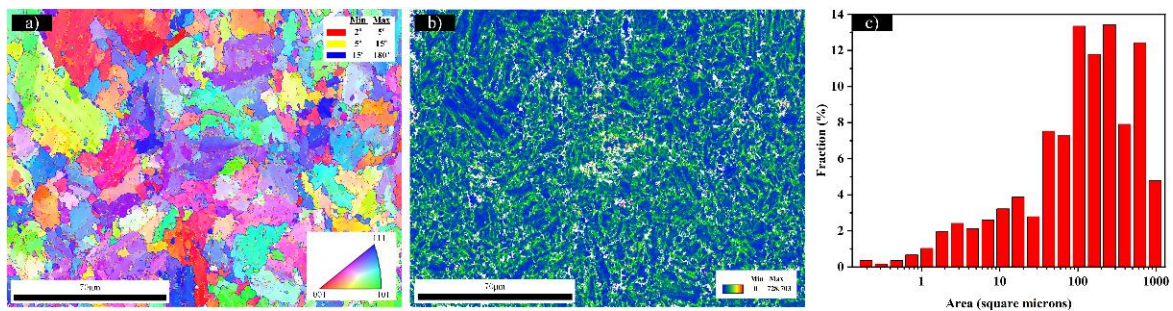


Figure 17. Microstructure information of sample D. (a) EBSD orientation map; (b) GND map; (c) grain area distribution.

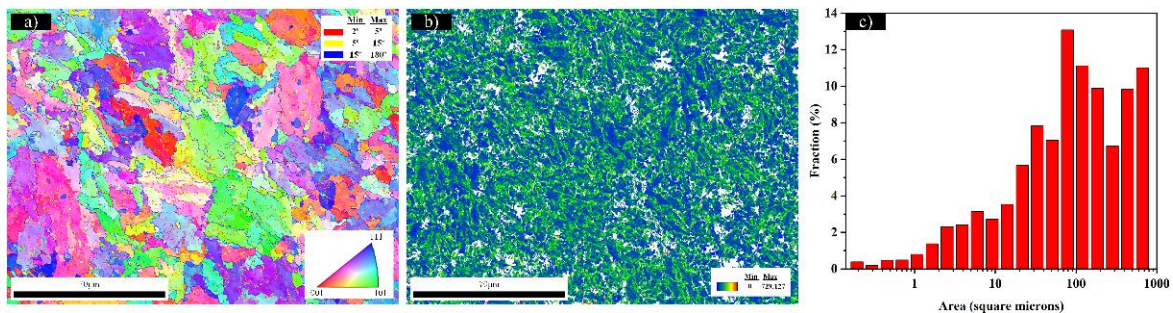


Figure 18. Microstructure information of sample E. (a) EBSD orientation map; (b) GND map; (c) grain area distribution.

From the overall point of view of heavy forgings, due to the heat treatment process, the mechanical properties of the outside of forgings are improved, and the hydrogen embrittlement sensitivity of materials is also improved. The external environment of forgings leads to the entry of convenient hydrogen on the surface of forgings, which makes it easier for forgings to undergo hydrogen embrittlement. Hydrogen will lead to a sharp decline in the mechanical properties of the outer layer of heavy forgings, and even produce crack sources in low stress environment, and the outer crack sources will cause stress concentration, resulting in rapid hydrogen-induced crack propagation to the core and sudden brittle fracturing, which is a serious threat to the service safety of large shaft parts. This is also a common form of hydrogen-induced failure of heavy forgings in engineering.

3.3. Discussion

Microstructure is the key to bringing about the differences in hydrogen embrittlement sensitivity. Combined with the microstructure and temperature change curve of sample groups A, B, C, D, and E, the hydrogen embrittlement sensitivity law was analyzed. It is well known that the existing forms and distribution of carbides are some of the important

differences between the above microstructures. Carbides in steel have an important influence on hydrogen embrittlement. The results show that the carbide interface can effectively trap hydrogen, and a larger carbide surface will bring more effective hydrogen traps [30]. Hydrogen traps can effectively pin diffusible hydrogen and change the distribution of hydrogen in the steel. In the martensite of point A, the size of carbides is large and unevenly distributed. This will lead to serious hydrogen segregation and greatly increase the local hydrogen concentration. The crack source is formed at the hydrogen enrichment site, which leads to the cracking of the material. On the contrary, homogeneous and dispersed carbides can effectively reduce hydrogen segregation and alleviate hydrogen embrittlement. It can be concluded that the hydrogen embrittlement sensitivity of martensite is higher than that of pearlite. This is similar to the results obtained by Michler et al. and Wan et al., who also found the same results in the study of hydrogen-induced cracking resistance of high strength low alloy steels [5,31]. It can be concluded that the martensite on the outside of the forging has high hydrogen embrittlement sensitivity.

In addition to microstructure, defects in steel also have an important influence on hydrogen embrittlement behavior. As an important hydrogen diffusion channel, more grain boundaries will significantly reduce the diffusion coefficient of hydrogen. According to the research of Chen and Park, the hydrogen concentration accumulated at the grain boundary of small-size grains is lower than that of large-size grains under the same variables, thus obtaining lower hydrogen embrittlement sensitivity [32–37]. Therefore, the smaller grain size of samples in group A will reduce the degree of hydrogen embrittlement to a certain extent. Unfortunately, it can be seen from Table 5 that group A has the highest hydrogen embrittlement sensitivity. The phenomenon of sample A may be considered by more microscopic factors. It can be seen from the EBSD and GND maps in Figure 14 that the small-angle grain boundaries in the grains of the A sample occupy a large area. Hydrogen traps and dislocations can pin hydrogen atoms in the diffusion process. The higher the dislocation density is, the higher the hydrogen content is. As a result, the hydrogen concentration accumulated in the lattice with high dislocation density is higher than that in the lattice with low dislocation density, which leads to higher hydrogen embrittlement sensitivity. In addition, dislocation also has significant influence on diffusion of hydrogen, Thus, the crack source is formed at the dislocation wall in the grain, and further propagates under the action of stress, resulting in transgranular fracture.

To sum up, a series of behaviors of hydrogen diffusion and adsorption in materials are closely related to the distribution of defects and carbonized second phase in steel, which comprehensively affect the hydrogen embrittlement behavior of steel. Only a single factor is considered to analyze the hydrogen embrittlement sensitivity is oversimplified. The hydrogen embrittlement sensitivity of heavy forgings is the result of the combined effect of microdefects and microstructure. Changing the distribution of carbides in the surface layer, as well as reducing the dislocation density and grain size, will contribute to the regulation of hydrogen embrittlement sensitivity. It is very important to customize the appropriate post-treatment process for its microstructure evolution.

4. Conclusions and Outlook

- (1) The thermophysical parameters of heavy forgings are obtained through experiments, and the temperature field distribution of heavy forgings is obtained by the finite element method. Guided by the temperature field distribution, the physical simulation experiment is completed, and a group of samples which conform to the radial distribution of heavy forging microstructure are obtained.
- (2) The results of electrochemical hydrogen charging and SSRT show that the martensite hardening layer on the edge of large parts has the highest hydrogen embrittlement sensitivity, while the fine pearlite and bainite nearby have much better resistance to hydrogen embrittlement.
- (3) Microstructure and EBSD orientation show that the hydrogen embrittlement sensitivity distribution is the result of the combined action of various microstructural features.

Different microstructures and grain sizes together affect the hydrogen embrittlement sensitivity of materials.

This study provides a method for the prediction of hydrogen embrittlement susceptibility of heavy parts. The temperature change curve of points A–E inside the large forging is obtained by FEM, and the corresponding heat treatment can be performed on each point to study the law of the overall structure of the forging with temperature. For similar projects, it provides a method for obtaining the microstructure of various internal points without cutting the processed material.

Author Contributions: L.L. participated in the formulation of the outline of the paper, data collection, model calculation, and manuscript writing; J.L. translated the manuscript and produced the pictures; Y.W. and G.Z. assisted in editing and reviewing the manuscript; F.D. provided financial support for this study, and participated in formulation of the outline of the paper. All authors have read and agreed to the published version of the manuscript.

Funding: This work was supported by the National Natural Science Foundation of China (51975510).

Data Availability Statement: The datasets generated during and/or analyzed during the current study are available from the first authors on reasonable request.

Conflicts of Interest: The author reports no competing interest. The authors are responsible for the content and writing of this paper.

References

1. Artola, G.; Aldazabal, J. Hydrogen Assisted Fracture of 30MnB5 High Strength Steel: A Case Study. *Metals* **2020**, *10*, 1613. [[CrossRef](#)]
2. Castens, M.; Hoja, S.; Surm, H.; Hoffmann, F.; Fechte-Heinen, R.; Steinbacher, M. Hydrogen Absorption during Case Hardening of Steels EN20MnCr5 (SAE5120) and EN18CrNiMo7-6 (SAE4820). *Metals* **2022**, *12*, 6. [[CrossRef](#)]
3. Fan, J.K.; Chen, H.T.; Zhao, W.; Yan, L. Study on Flake Formation Behavior and Its Influence Factors in Cr5 Steel. *Materials* **2018**, *11*, 690. [[CrossRef](#)] [[PubMed](#)]
4. Jiang, J.J.; Lin, Z.Y.; Feng, M.L.; Meng, X.-Q.; Cai, X.-J.; Liu, F. Experimental study on temperature influence to fracture toughness of Cr5 cold roll steel. *Forg. Stamp. Technol.* **2012**, *37*, 135–139.
5. Michler, T.; Naumann, J. Microstructural aspects upon hydrogen environment embrittlement of various bcc steels. *Int. J. Hydrogen Energy*. **2010**, *35*, 821–832. [[CrossRef](#)]
6. Bechtle, S.; Kumar, M.; Somerday, B.P.; Launey, M.E.; Ritchie, R.O. Grain-boundary engineering markedly reduces susceptibility to intergranular hydrogen embrittlement in metallic materials. *Acta Mater.* **2009**, *57*, 4148–4157. [[CrossRef](#)]
7. Ji, S.K.; You, H.L.; Lee, D.L.; Park, K.T.; Chong, S.L. Microstructural influences on hydrogen delayed fracture of high strength steels. *Mater. Sci. Eng. A* **2009**, *505*, 105–110.
8. Kimura, Y.; Takagi, S.; Hara, T.; Terasaki, S.; Tsuzaki, K. Hydrogen-induced delayed fracture of a martensitic steel with fine prior-austenite grain size. *J. Phys. IV* **2003**, *112*, 403–406. [[CrossRef](#)]
9. Jeffrey, V.; Zhou, Q.J.; Liu, Q.L.; Li, H.X.; Zhang, M.X.; Matthew, D.; Andrel, A. The influence of microstructure on the hydrogen embrittlement susceptibility of martensitic advanced high strength steels. *Mater. Today Commun.* **2018**, *17*, 1–14.
10. Cong, Z.; Murata, Y. Dislocation Density of Lath Martensite in 10Cr-5W Heat-Resistant Steels. *Mater. Trans.* **2011**, *52*, 2151–2154. [[CrossRef](#)]
11. Bollinger, A.; Murakami, T.; Findley, K.; Emmanuel, D.M.; Speer, J. The Influence of Microstructural Variations on Hydrogen Absorbance and Tensile Properties at Elevated Hydrogen Levels for TRIP-Aided Bainitic Ferrite Steels. *Corrosion* **2018**, *75*, 888–897. [[CrossRef](#)]
12. Martin, M.L.; Fenske, J.A.; Liu, G.S.; Sofronis, P.; Robertson, I.M. On the formation and nature of quasi-cleavage fracture surfaces in hydrogen embrittled steels. *Acta Mater.* **2011**, *59*, 1601–1606. [[CrossRef](#)]
13. Hejazi, D.; Haq, A.J.; Yazdipour, N.; Dunne, D.P.; Calka, A.; Barbaro, F.; Pereloma, E.V. Effect of manganese content and microstructure on the susceptibility of X70 pipeline steel to hydrogen cracking. *Mater. Sci. Eng. A* **2012**, *551*, 40–49. [[CrossRef](#)]
14. Marchi, C.S.; Ronevich, J.A.; Sabisch, J.E.C.; Sugar, J.D.; Somerday, B.P. Effect of microstructural and environmental variables on ductility of austenitic stainless steels. *Int. J. Hydrog. Energy* **2021**, *46*, 12338–12347. [[CrossRef](#)]
15. Hughes, L.A.; Somerday, B.P.; Balch, D.K.; Marchi, C.S. Hydrogen compatibility of austenitic stainless steel tubing and orbital tube welds. *Int. J. Hydrog. Energy* **2014**, *39*, 20585–20590. [[CrossRef](#)]
16. Toribio, J.; Vergara, D.; Lorenzo, M. Hydrogen effects in multiaxial fracture of cold-drawn pearlitic steel wires. *Eng. Fract. Mech.* **2017**, *174*, 243–252. [[CrossRef](#)]
17. Toribio, J.; Vergara, D. Role of microstructural anisotropy in the hydrogen-assisted fracture of pearlitic steel notched bars. *Int. J. Fract.* **2013**, *182*, 149–156. [[CrossRef](#)]

18. Duan, H.Q.; Han, Y.F.; Lv, W.J.; Mao, J.W.; Wang, L.Q.; Zhang, D. Effect of solid carburization on surface microstructure and hardness of Ti-6Al-4V alloy and (TiB+La₂O₃)/Ti-6Al-4V composite. *Trans. Nonferrous Met. Soc.* **2016**, *26*, 1871–1877. [[CrossRef](#)]
19. Skubisz, P.; Lisiecki, L. Warm-forging characteristics and microstructural response of medium-carbon high-strength steels for high-duty components. *Key Eng. Mater.* **2014**, *611*, 167–172. [[CrossRef](#)]
20. Roumina, R.; Emburry, J.D.; Bouaziz, O.; Zurob, H.S. Mechanical behavior of a compositionally graded 300M steel. *Mater. Sci. Eng. A* **2013**, *578*, 140–149. [[CrossRef](#)]
21. Skubisz, P.; Sinczak, J. Properties of direct-quenched aircraft forged component made of ultrahigh-strength steel 300M. *Aircr. Eng. Aerosp. Tec.* **2018**, *90*, 713–719. [[CrossRef](#)]
22. Hoseiny, H.; Klement, U.; Sotkovszki, P. Comparison of the microstructures in continuous-cooled and quench-tempered pre-hardened mould steels. *Mater. Des.* **2011**, *32*, 21–28. [[CrossRef](#)]
23. Luo, J.; Li, M.Q.; Liu, Y.G.; Sun, H.M. The deformation behavior in isothermal compression of 300M ultrahigh-strength steel. *Mater. Sci. Eng. A* **2012**, *534*, 314–322. [[CrossRef](#)]
24. Zhu, X.; Zhang, K.; Li, W.; Jin, X.J. Effect of retained austenite stability and morphology on the hydrogen embrittlement susceptibility in quenching and partitioning treated steels. *Mater. Sci. Eng. A* **2016**, *658*, 400–408. [[CrossRef](#)]
25. Pola, A.; Vecchia, G.M.L.; Zola, F. Computer simulation of the heat treatment process applied to a forged shaft. *Metall. Ital.* **2010**, *102*, 5–11.
26. Zhang, J.; Cui, Z.S. Investigation for measuring heat transfer coefficient on contact surface of hot forgings. *J. Plast. Eng.* **2015**, *22*, 32–39.
27. Yang, X.; Sun, F.; Li, Q.; Zhu, R.; Liu, Z.; Du, C.; Li, X. Effect of Hydrogen Charging on the Stress Corrosion Cracking Behavior of X70 Steel in Simulated Deep Seawater Environment. *Metals* **2022**, *12*, 334. [[CrossRef](#)]
28. Toribio, J.; Vergara, D.; Lorenzo, M. Influence of Loading Rate on the Hydrogen-Assisted Micro-Damage in Bluntly Notched Samples of Pearlitic Steel. *Metals* **2016**, *6*, 11. [[CrossRef](#)]
29. Wang, M.Q.; Akiyama, E.J.; Tsuzakia, K. Crosshead speed dependence of the notch tensile strength of a high strength steel in the presence of hydrogen. *Scr. Mater.* **2005**, *53*, 713–718. [[CrossRef](#)]
30. Gao, X.Z.; Yue, F.L.; Xu, B.; He, X. Quality control of local loading forming for a large aviation aluminum alloy forging. *Forg. Stamp. Technol.* **2017**, *42*, 1–5.
31. Chen, Y.S.; Lu, H.; Liang, J.; Rosenthal, A.; Liu, H.; Sneddon, G.; Mccarroll, I.; Zhao, Z.; Li, W.; Guo, A. Observation of hydrogen trapping at dislocations, grain boundaries and precipitates. *Science* **2020**, *367*, 171–175. [[CrossRef](#)]
32. Wan, K.K.; Koh, S.U.; Yang, B.Y.; Kim, K.Y. Effect of environmental and metallurgical factors on hydrogen induced cracking of HSLA steels. *Corros. Sci.* **2018**, *50*, 3336–3342.
33. Chen, S.; Zhao, M.; Rong, L. Effect of grain size on the hydrogen embrittlement sensitivity of a precipitation strengthened Fe-Ni based alloy. *Mater. Sci. Eng. A* **2014**, *594*, 98–102. [[CrossRef](#)]
34. Bai, Y.; Momotani, Y.; Chen, M.C.; Shibata, A.; Tsuji, N. Effect of grain refinement on hydrogen embrittlement behaviors of high-Mn TWIP steel. *Mater. Sci. Eng. A* **2016**, *651*, 935–944. [[CrossRef](#)]
35. Park, I.J.; Lee, S.M.; Jeon, H.H.; Lee, Y.K. The advantage of grain refinement in the hydrogen embrittlement of Fe-18Mn-0.6C twinning-induced plasticity steel. *Corros. Sci.* **2015**, *93*, 63–69. [[CrossRef](#)]
36. Tsay, L.W.; Lu, H.L.; Chen, C. The effect of grain size and aging on hydrogen embrittlement of a maraging steel. *Corros. Sci.* **2008**, *50*, 2506–2511. [[CrossRef](#)]
37. Mine, Y.; Horita, N.; Horita, Z.; Takashima, K. Effect of ultrafine grain refinement on hydrogen embrittlement of metastable austenitic stainless steel. *Int. J. Hydrog. Energy* **2017**, *42*, 15415–15425. [[CrossRef](#)]